INTERNATIONAL JOURNAL OF
INFORMATION AND SYSTEMS SCIENCES
Volume 3, Number 2, Pages 292-306

A COMPARATIVE STUDY OF 3D ELECTRICAL CAPACITANCE TOMOGRAPHY

MANUCHEHR SOLEIMANI[1], HAIGANG WANG[2], YI LI[2] AND WUQIANG YANG[2]

Abstract. Electrical capacitance tomography (ECT) attempts to visualise the permittivity distribution by measuring capacitance between pairs of electrodes, which are placed around the periphery of a cross section. The difficulty with image reconstruction for ECT is that the relationship between capacitance and permittivity is nonlinear and the inverse problem is ill-posed and ill-conditioned. 3D ECT has been studied in the past few years and is more challenging than 2D ECT. In this paper 3D images reconstructed by both linear and nonlinear image reconstruction methods are presented. Various scenarios for 3D ECT imaging with different sensors are discussed, e.g. with an increased number of electrodes and projections. The results show improved image quality using complete 3D measurement data.

Keywords: Electrical capacitance tomography, forward and inverse problems, 3D images, image reconstruction

1. Introduction

Electrical capacitance tomography (ECT) is a relatively mature imaging modality of industrial process tomography [11] [12] [13] [14]. The aim of ECT is to visualise the distribution of dielectric materials with a contrast in permittivity, by measuring capacitance from a set of electrodes. Applications of ECT include the measurement of oil-gas flows in pipelines and gas-solids flows in pneumatic conveying [1].

A typical ECT sensor comprises an array of conducting plate electrodes, which are mounted on the outside of a non-conducting pipe, and surrounded by an electrical shield. For a metal wall pipe or vessel, the sensing electrodes must be mounted internally, with an insulation layer between the electrodes and the metal wall and using the metal wall as the electrical shield. Other components in the sensor include radial and axial guard electrodes, which are arranged to reduce the external coupling capacitance between the electrodes and to achieve an improved signal-to-noise ratio and hence improved image quality. As usually the measurement electrodes do not physically contact with the materials being measured, ECT provides a non-intrusive and non-invasive means, avoiding intervene and contamination of the materials.

Image reconstruction in ECT is a nonlinear, ill-posed and ill-conditioned inverse problem [3] [5] [6] [7] [9]. While most ECT systems can only generate 2D images, there has been a growing interest in 3D ECT in the past few years, e.g. in Ohio State University, Technical University of Lodz (Poland) and the University of Manchester [8] [10] [15]. In this paper new 3D image reconstruction methods for ECT and new results obtained using the new methods are presented [15]. In particular, 3D ECT with different number of electrodes, different number of planes of electrodes and different projections has been studied, with various sensor structures:

Received by the editors in revised form January 19, 2007

(1) 8 round electrode sensor
(2) Single-plane 8-electrode sensor
(3) Twin-plane sensor with 8 electrodes in each plane, 16 electrodes in total
(4) Three-plane sensor with 12 electrodes in each plane, 36 electrodes in total
(5) Four-plane sensor with 8 electrodes in each plane, 32 electrodes in total
(6) 24-electrode true 3D sensor
(7) 54-electrode true 3D sensor

As expected, the 54-electrode true 3D ECT sensor providing complete measurement data ensures the best image quality.

2. 3D ECT sensors

Figure 1 shows a typical 2D ECT sensor with 8 measurement electrodes. It also indicates the electric field lines inside the sensor, where only one electrode is applied a voltage $\varphi = V_0$ and others are set to zero. Figures 2-5 show various sensors used in this study for investigation of 3D ECT.

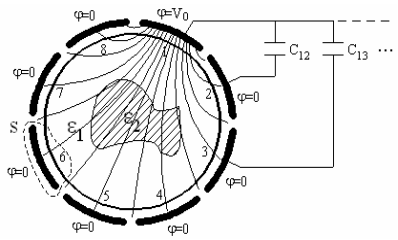

Figure 1: Typical 2D ECT sensor

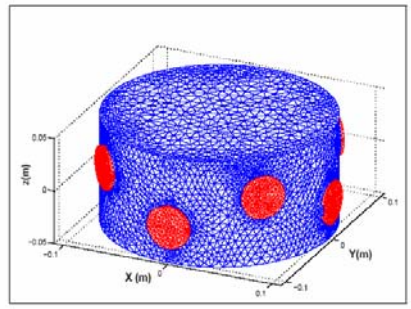

Figure 2: 8 round electrode sensor with FE mesh shown

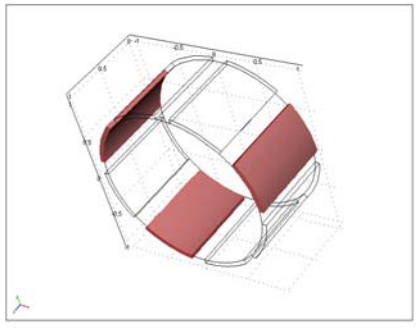

(a) Single-plane 8-electrode sensor

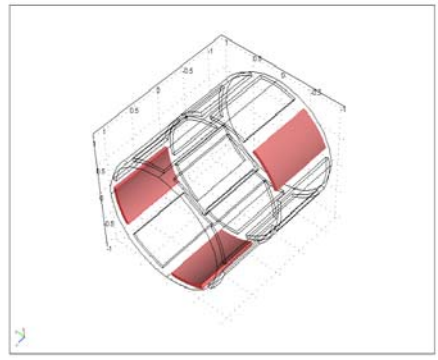

(b) Twin-plane sensor with 8 electrodes in each plane, 16 electrodes in total

Figure 3: Round pipeline sensors

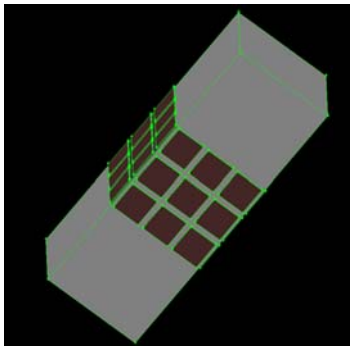

(a) Three-plane sensor with 12 electrodes in each plane, 36 electrodes in total

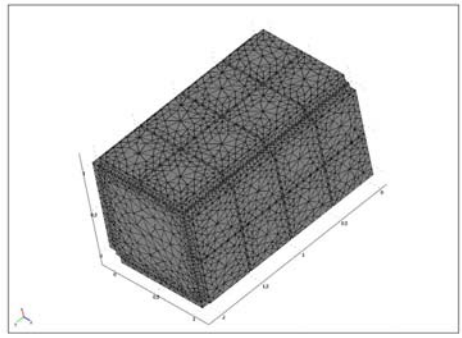

(b) Four-plane sensor with 8 electrodes in each plane, 32 electrodes in total

Figure 4: Multi-plane square pipeline sensors

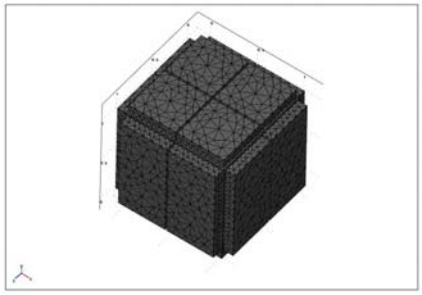

(a) 24-electrode true 3D model with FE mesh shown

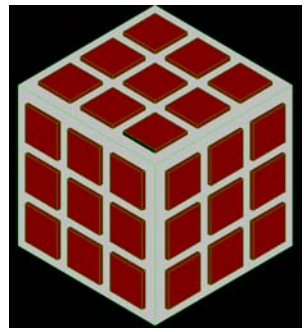

(b) 54-electrode true 3D sensor

Figure 5: True 3D sensors, providing complete measurement data

3. Forward problem

The forward problem in ECT is to estimate capacitance for given geometry information of a sensor, the applied potential and the permittivity distribution in a cross section. While the conventional arrangement is to use a single electrode for excitation and a single electrode for detection, different measurement protocols have been attempted, e.g. a combination of electrodes for excitation. With the conventional protocol, each of the electrodes is set to some potential in turn, and the others remain zero potential. The charge is measured on each of zero-potential electrodes.

3.1 Finite element method

In general, the Maxwell's equations need to be solved for the forward problem. With a low frequency, wave propagation and electromagnetic interferes may be ignored. With a high frequency a more complicated model than for a low frequency is needed. In a

simplified mathematical model, the electrostatic approximation $\nabla \times E = 0$ is taken, effectively ignoring the effect of wave propagation. Let's take $E = -\nabla u$ and assume no internal charges. Then the following equation holds.

(1) $$\nabla \cdot \varepsilon \nabla u = 0 \quad in \ \ \Omega$$

where *u* is the electric potential and Ω is the region containing the electric field.

The potential on each electrode is known as

(2) $$u = v_k \ \ ek$$

where ε is the permittivity, *ek* is the *k*-th electrode held at the potential v_k, and **n** is the normal on the surface [5].

To solve equation (1) together with equation (2) numerically, the domain is partitioned into *k* tetrahedral with a total of *n* vertices. The permittivity coefficients are each approximated by a piecewise constant function on that mesh. Given a standard nodal basis $\{\phi_i\}_{i=1}^{n}$ for the set of piecewise linear functions, a potential is sought in the form,

(3) $$u_h = \sum_{i=1}^{n} u_i \phi_i$$

Multiplying the Poisson equation by an arbitrary but sufficiently smooth test function *v* and integrating over Ω gives

(4) $$\int_{\Omega} v \nabla \cdot (\varepsilon \nabla u_h) dx^3 = 0$$

By partial integration, the following equation is obtained.

(5) $$\int_{\Omega} \varepsilon \nabla u_h \cdot \nabla v dx^3 = \int_{\Gamma_1} \varepsilon \nabla u_h \cdot \tilde{n} v dx^2 + \int_{\Gamma 2} \varepsilon \nabla v \cdot \tilde{n} u_h dx^2$$

Assuming $K(i,j) = \int_{\Omega} \varepsilon \nabla \phi_i \cdot \nabla \phi_j dx^3 \qquad i, j = 1:n$, a linear system of equations is obtained as

(6) $$K(\varepsilon) U = B$$

where the matrix ***K*** is the discrete representation of the operator $\nabla \cdot \varepsilon \nabla$, the vector ***B*** is the boundary condition term and ***U*** is the vector of electric potential solution.

The electric charge on the *k-th* electrode is given by

(7) $$Q_k = \int_{E_k} \varepsilon \frac{\partial u}{\partial n} dx^2$$

where ***n*** is the inward normal on the *k*-th electrode.

In an ECT system the capacitance data are usually normalised by calibration date [18] and are given by $\lambda = \frac{C_{meas} - C_{air}}{C_{high} - C_{air}}$, where C_{air} is the capacitance measurement when the sensor is empty, C_{high} is the capacitance measurement when the sensor is full of a high permittivity material and C_{meas} is the absolute capacitance measurement. As shown in Figures 2, 4 (b) and 5 (a), an FE mesh is usually used to obtain a numerical solution for a given ECT sensor. Note that the exterior shield is considered in each of the models but is not shown in the FE meshes.

To obtain the sensitivity the Frechet derivative of the measured capacitance is calculated with respect to a perturbation in permittivity. A simple approach is to ignore the higher order terms. This can simply be extended to a formal proof using the Operator series. A derivation of sensitivity formula was given in [6]. To obtain the change in Q on electrode E_i when E_j is driven, the potential u_i is applied when electrode E_i is driven and u_j when E_j is driven. The sensitivity formula is as follows.

$$\delta Q_{ij} = \int_{\Omega_k} \delta\varepsilon \nabla u_i \cdot \nabla u_j dx^3 \tag{8}$$

where Ω_k is the perturbed region, and ∇u_i and ∇u_j can be calculated by the solution to the forward problem when electrodes *i* and *j* are excited.

3.2 Finite volume method

In this study a finite volume method (FVM) has been developed to solve the forward problem for 3D ECT. Due to the difficulty in finding an analytical solution, FEM or FVM is often used. Take the 3D cube sensor with 9 electrodes in each side as an example (see Figure 5 (b)). For this sensor, FVM is more convenient for solving the Laplace equation than FEM, because FEM is normally performed using a triangle mesh, while FVM is based on a cubic mesh [5]. The differential equation in FVM is

$$u(i,j) = \frac{\varepsilon_E u(i+1,j) + \varepsilon_W u(i-1,j) + \varepsilon_N u(i,j+1) + \varepsilon_S u(i,j-1)}{\varepsilon_E + \varepsilon_W + \varepsilon_N + \varepsilon_S} \tag{9}$$

where

$$\varepsilon_E = \varepsilon(i,j) + \varepsilon(i,j-1)$$

$$\varepsilon_W = \varepsilon(i-1,j-1) + \varepsilon(i-1,j)$$

$$\varepsilon_N = \varepsilon(i-1,j) + \varepsilon(i,j-1)$$

$$\varepsilon_S = \varepsilon(i,j-1) + \varepsilon(i-1,j-1)$$

To speed up the iterative process, a relaxation factor is introduced and the iterative forum is

$$u^{n+1}(i,j) = \varpi \cdot u^{n}(i,j) + (1-\varpi) \cdot u(i,j) \tag{10}$$

The sensing volume is divided into $54 \times 54 \times 54$ hexahedron cells. A 2nd order central differencing scheme is used in calculation [16] and a program is written in Fortran'95. The procedures of calculation are summarised as follows. A voltage is applied to a source electrode and the remaining electrodes are kept at the earth potential. An iterative approach is used to solve the potentials over the whole domain. In principle, 54 potential distributions should be found for each of the electrodes. In practice, however, only 3 typical potential distributions are needed. All the other potential distributions can be obtained simply by mirroring and rotating, significantly reducing computation time. Figure 6 shows three typical potential distributions in 3D for three typical situations: (a) when an electrode in corner is energised, (b) when an electrode in middle along edge is energised and (c) when an electrode in centre of one side is energised.

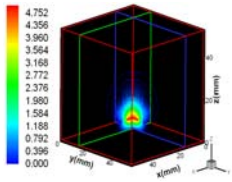

(a) Electrode in corner is energised

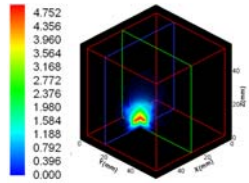

(b) Electrode in middle along edge is energised

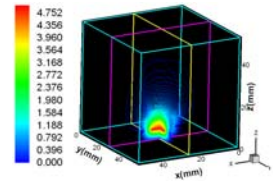

(c) Electrode in centre of one side is energised

Figure 6: Typical potential distributions calculated using FVM

The sensitivity map of electrode pair *i-j* at a spatial location (*x,y,z*) can now be calculated by vector multiplication of two electric fields, which are normal to the potential distributions.

$$J_{i,j}(x,y,z) = -\oint_{p(x,y,z)} \frac{\overrightarrow{E_i}}{V_i} \cdot \frac{\overrightarrow{E_j}}{V_j} dv = -\oint_{p(x,y,z)} \left(\frac{\partial u_i}{\partial x} \cdot \frac{\partial u_j}{\partial x} + \frac{\partial u_i}{\partial y} \cdot \frac{\partial u_j}{\partial y} + \frac{\partial u_i}{\partial z} \cdot \frac{\partial u_j}{\partial z}\right) dxdydz \tag{11}$$

where *E(x,y,z)* is the electric field distribution when an excitation voltage V_i is applied to electrode *i* while all other electrodes remain at the earth potential, and *p(x,y,z)* is the volume of the cell at (*x,y,z*).

As there are 1431 independent capacitance measurements, 1431 sensitivity maps are needed in principle. Because of symmetry, however, there are only 4 typical sensitivity maps as shown in Figure 7, indicating the high sensitivity between neighbouring electrodes, such as electrode pair 2-5 (in the order of $-10e-3 \sim +10e-2$) and low sensitivity between opposing electrodes, such as electrode pair 5-23 (in the order of $-10e-5 \sim +10e-4$). Also, the symmetric feature can be seen clearly in Figure 7 (d) for the opposing electrode pair 5-23.

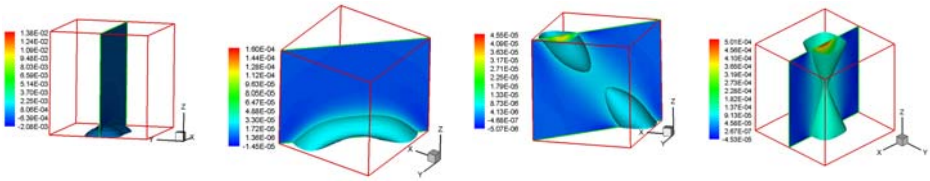

(a) Electrodes 2-5 (b) Electrode 2-8 (c) Electrodes 1-27 (d) Electrodes 5-23

Figure 7 Typical sensitivity maps calculated by vector multiplication of electric field distributions

Having obtained the typical sensitivity maps ($J_{i,j}, i=1,\ldots,9, j=i+1,\ldots 54$), other sensitivity maps ($J_{i,j}, i=10,\ldots,53, j=i+1,\ldots 54$) can be obtained simply by mirroring and rotating. In total 1431 sensitivity maps are obtained. The next task is to use the sensitivity maps for image reconstruction.

4. Image reconstruction

4.1 Linear reconstruction

To demonstrate true 3D image reconstruction with complete measurement data, capacitance "measurements" were obtained from the sensor model as shown in Figure 5 (b), using an FEM software package Maxwell from Ansoft [2]. The measurement sequence was as follows. First, electrode 1 is energised and "measurements" are taken from electrodes 2 to 54. Then electrode 2 is energised and "measurements" are taken from electrodes 3 to 54, and so on, until electrode 53 is energised and a single "measurement" is taken from electrode 54. In total, there are 1431 independent capacitance "measurements".

Linear back-projection (LBP) is a simple image reconstruction algorithm and has commonly been used in ECT for 2D image reconstruction. For 3D images reconstruction, it takes a similar format to the 2D case and is given by

$$G(x,y,z) = \sum_{i=1}^{N-1}\sum_{j=i+1}^{N} C_{ij}J_{ij}(x,y,z) \Big/ \sum_{i=1}^{N-1}\sum_{j=i+1}^{N} J_{ij}(x,y,z) \tag{12}$$

where, $G(x,y,z)$ is the grey level in a pixel (x,y,z), i.e. the reconstructed image, C_{ij} is the normalised capacitance, which in this case was obtained using FEM simulation software, and N is the number of electrodes.

To obtain high quality images, the Landweber iteration algorithm has been implemented for image reconstruction [13] and is given by

$$G^{(n+1)} = G^{(n)} + \alpha J^T (C - JG^{(n)}), (n = 1,2,3,\cdots) \tag{13}$$

In this algorithm the first image vector $G^{(0)}$ is reconstructed using equation (12). Each subsequent image vector $G^{(k+1)}$ is obtained from the previous image $G^{(k)}$ with an added

correction term $\alpha J^T (C - JG^{(k)})$. In equation (13), $C - JG^{(k)}$ is the error between the measured capacitance vector *C* and a re-calculated capacitance vector $JG^{(k)}$. The error is used to reconstruct the next image. The relaxation factor α will be discussed in the next part.

4.2 Nonlinear reconstruction

In the regularised Gauss-Newton method the second order term in the Hessian is approximated [6] [7] [8] [14]. The regularised optimisation is to find ε, given ε0 as the initial guess and $R\varepsilon$ as the regularisation function. A regularisation parameter λ can be included so that the cost functional is

$$g(\varepsilon) = \|C - F(\varepsilon)\| + \lambda^2 R \tag{14}$$

where *C* is the measured capacitances and *F* is the forward map. For the regularised Gauss-Newton method, the iteration steps are

$$\varepsilon_{i+1} = \varepsilon - H(\varepsilon_i)^{-1} \nabla g(\varepsilon_i) \tag{15}$$

$$H(\varepsilon_i) = F'(\varepsilon_i)^T F'(\varepsilon_i) + \lambda^2 R''(\varepsilon_i) \tag{16}$$

where *H* is the modified Hessian and *R* is regularisation function and

$$\nabla g(\varepsilon_i) = F'(\varepsilon_i)(F(\varepsilon_i) - C) + \lambda^2 R'(\varepsilon_i) \tag{17}$$

where $R'(\varepsilon_i)$ and $R''(\varepsilon_i)$ are the first and second derivatives of $R(\varepsilon_i)$. with respect to ε_i.

In order to deal with the ill-conditioning problem, it needs to be regularised, by incorporating additional information about the solution. A choice is by discrete approximation to the Laplace operator, in which case the penalty term is

$$R(\varepsilon_i) = \int_{\Omega} \left| \nabla(\varepsilon - \varepsilon_{ref} \right|^2 dx \tag{18}$$

If the element *l* has at least one vertex in common with $n_1, n_2, ..., n_i$ then $R(l, n_1, n_2, ..., n_i) = -1$ and $R(l,l) = \sum R(l, n_i)$.

The matrix *R* is a regularisation matrix to penalise extreme changes in permittivity, removing the instability in reconstruction, at the cost of producing artificially smooth images. In a discrete form the iteration steps are

$$\Delta\varepsilon_i = (J_i^T J_i + \lambda^2 R^T R)^{-1} J_i^T ((C - F(\varepsilon_i)) - \lambda^2 R^T R(\varepsilon_i - \varepsilon_0)) \tag{19}$$

For $i = 1$ this is a linear reconstruction algorithm. Here J_i is the Jacobian calculated for the inverse parameter ε_i, *C* is the vector of measurements and the forward solution

$F(\varepsilon_i)$ is the predicted measurement from the forward model with parameter ε_i. The iteration is stopped when $\|C - F(\varepsilon_i)\| < er$, where er is the estimated noise level in the measurement system.

5. Simulation results and discussions

5.1 Nonlinear reconstruction with 8 electrodes sensor

The nonlinear algorithm described in section 4.2 has been used for image reconstruction. The data were generated using a different FE mesh and 1% noise was added to the simulated data. Figure 8 (a) shows a reconstructed image of a single sphere (permittivity 1.3) of 2 cm in diameter and its centre at (4,0,2) cm. Figure 8 (b) shows a reconstructed image of two spheres (permittivity 1.8) in two sides of plane Z = 0. The spheres are 1 cm in diameter and are placed their centres at (-4,0,3) cm and (+4,0,-3) cm. The region for image reconstruction is divided into 2800 tetrahedral elements and the regularisation parameter was chosen to be 10e-9. It can be seen from Figure 8 (b) that the two spheres are located correctly and their size is correct. However, due to noise and the nature of the ill-posed inverse problem, their shape is not exactly spherical.

(a) A single sphere (b) Two spheres

Figure 8: Reconstructed images by 8-electrode sensor as shown in Figure 2

5.2 Reconstruction with and without top and bottom electrodes

For comparison purposes, a three-plane ECT sensor with 12 electrodes in each plane is designed as shown in Figure 4 (a). Its electrodes are the same in geometry, size and shape as those in Figure 5 (b). The difference is that there are no electrodes in the top and bottom sides. With the sensor shown in Figure 4 (a), there are 3 × 12 = 36 electrodes in total, which are mounted around a rectangle pipe. This sensor gives 35 × 18 = 630 independent measurements. The aim of designing this sensor is to verify the role of the top and bottom electrodes in 3D image reconstruction. The 36-electrode sensor gives incomplete measurement data because there are no measurements from the top and the bottom sides.

To compare the quality of reconstructed images using complete measurement data from the 54-electrode sensor as shown in Figure 5 (b), with that using incomplete measurement data from the 36-electrode sensor as shown in Figure 4 (a), two cases were tested: (1) a single sphere was placed in four positions in the measurement volume and

(2) two spheres in opposite corners. Capacitance data were obtained using FEM simulation software.

Figure 9 shows the reconstructed images of one sphere in different positions with both complete and incomplete measurement data. The position is defined by a ratio *z/L*. *z/L* = 0 means that the sphere is in the centre and *z/L* = 1 means that the sphere is on the wall. All the images are reconstructed with 20 iterations. It can be seen from Figure 9 that with the 54-electrode sensor, the shape of the reconstructed sphere is the same in different positions from *z/L* = 0 to *z/L* = 0.75. With the 36-electrode sensor, however, the shape of the reconstructed sphere is distorted, from sphere to ellipsoid. If the sphere is placed further away from the centre, the more distortion the image is. In the position of *z/L* = 0.75, which is close to the top plane of the sensor, it is very difficult to reconstruct a good image with incomplete measurement data, presenting an image error nearly 100%. This can be seen more clearly in terms of image errors and sphericity coefficient as shown in Figure 10. For the 54-electrode sensor, the sphericity coefficient nearly keeps constant and is closed to the real sphere diameter, which varies in the range of 0.95 and 1.05. For the 36-electrode sensor, however, the sphericity coefficient changes significantly in different position. The image error increases with the increase of *z/L*.

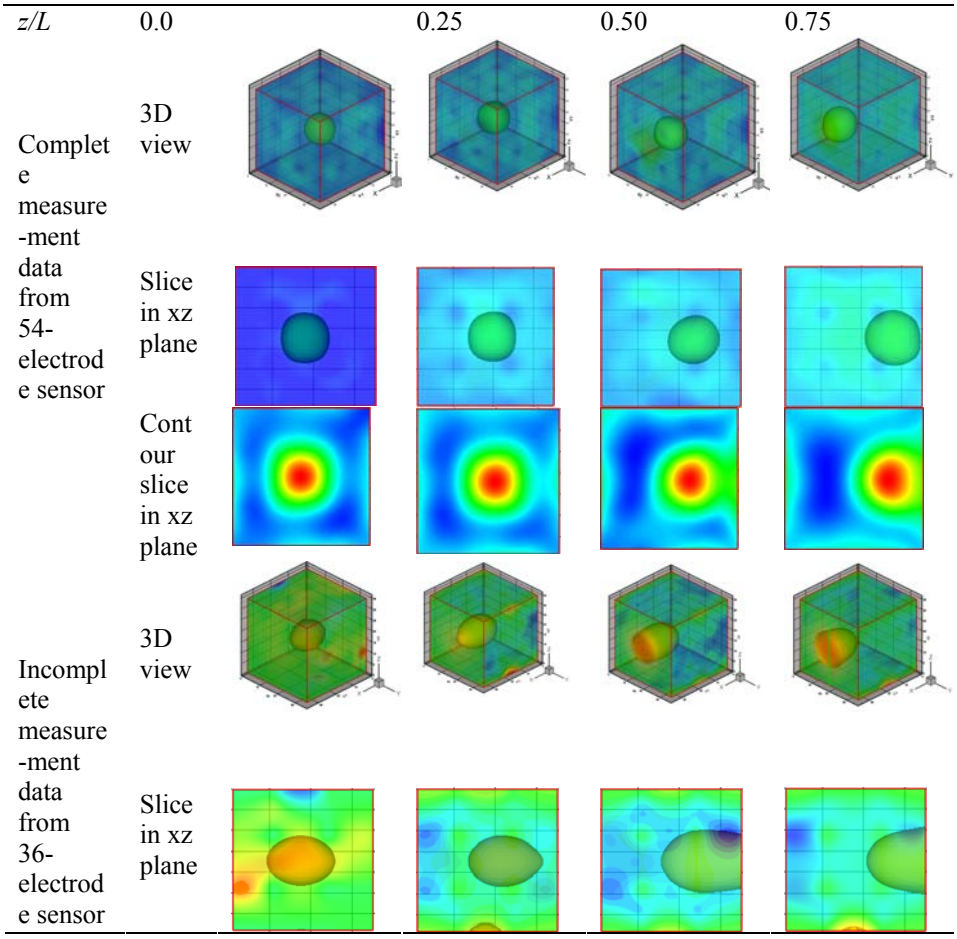

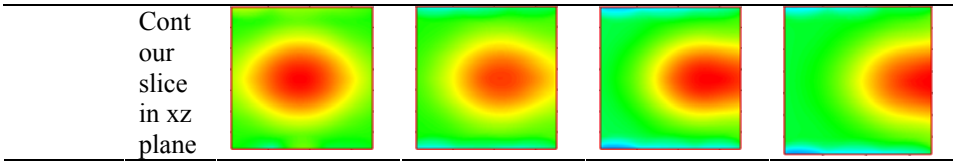

Figure 9: Reconstructed images of one sphere, using 54-electrod sensor as shown in Figure 5 (b)
and 36-electrode sensor as shown in Figure 4 (a)

From the results, it is clear that the top and bottom electrodes play an important role in 3D image reconstruction. Without these electrodes, the measurement data is incomplete and the reconstructed images are distorted if the sphere(s) is not exactly in the centre. Therefore, true 3D image cannot be reconstructed using incomplete measurement data. In terms of image quality, the 54-electrode sensor is much better than the 36-electrode sensor. In terms of application, however, the 54-electrode sensor is more limited than the 36-electrode sensor because it cannot be used for flow measurement.

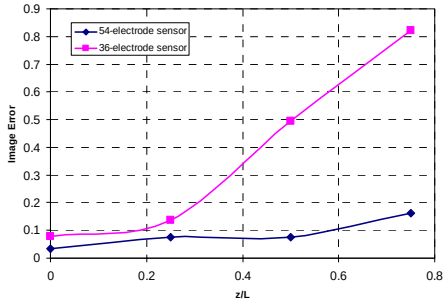

(a) Image error

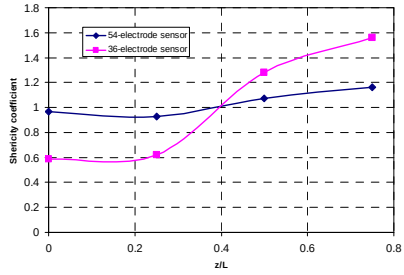

(b) Sphericity coefficient of image

Figure 10: Comparison of 54-electrode sensor (Figure 5 (b)) with
36-electrode sensor (Figure 4 (a))

A further test was carried out with two spheres in opposite corners as shown in Figure 11 (a). Figure 11 (b) shows the reconstructed images both with complete and incomplete measurement data, using different algorithms. With the 54-electrode sensor, good-quality images can be reconstructed by LBP. With the 36-electrode sensor, however, iteration is necessary to obtain good quality images, say 20 iterations. After iterations, the shape of the reconstructed sphere keeps the same with 54-electrode sensor. With the 36-electrode sensor, however, the change is obvious as shown in Figure 11 (b). In the both cases, the image noise becomes noticeable with the increase of the number of iterations. There are two main possible reasons for this. Firstly, the accuracy of the simulated capacitance data using the software is not high and small measurement errors can result in divergence due to a very large condition number. Secondly, the image reconstruction algorithm is rather simple. A suitable algorithm is necessary for true 3D image reconstruction, in particular with a very large condition number.

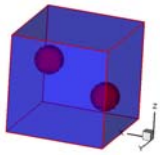

(a) True distribution

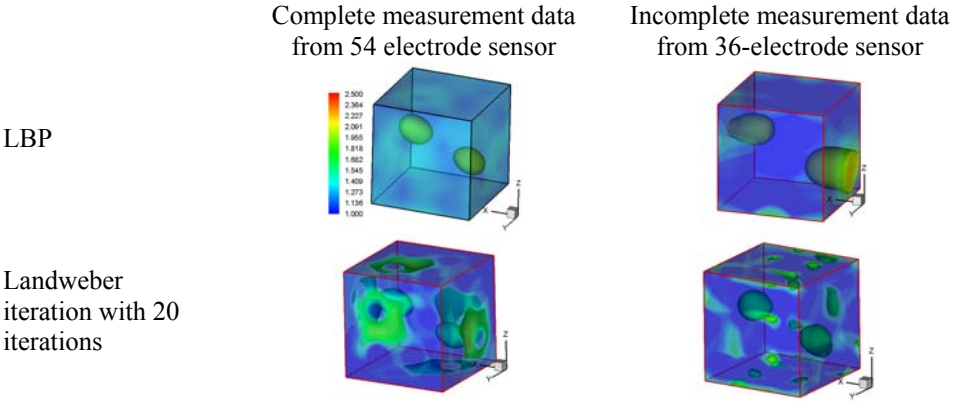

(b) Reconstructed images

Figure 11: 3D image reconstruction with 36-electrode sensor (Figure 4 (a)) and 54-electrode sensor (Figure 5 (b))

5.3 Reconstruction with pipeline sensors

Figures 12 show simulation results with the round pipeline sensors as shown in Figures 3 (a) and (b) respectively.

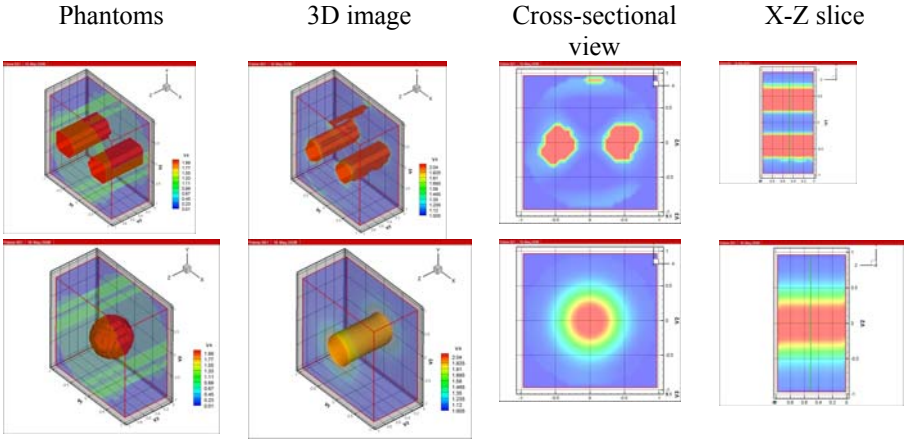

(a) Image reconstruction using single-plane 8-electrode round pipeline sensor shown in Figure 3 (a)

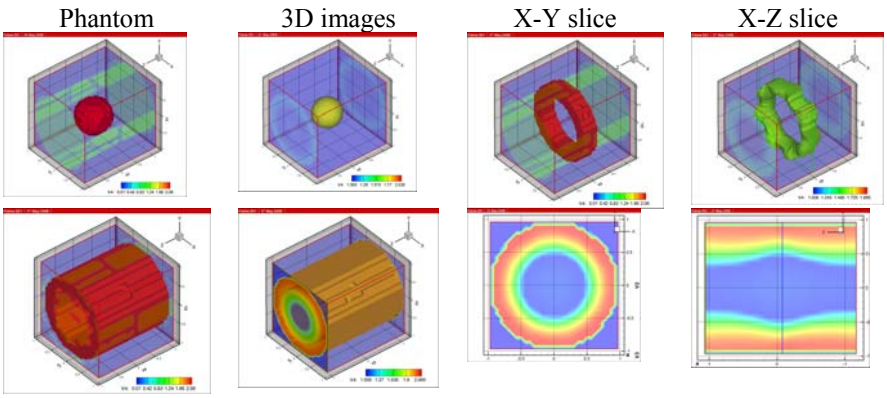

(b) Image reconstruction with twin-plane round pipeline sensor shown in Figure 3 (b)

Figure 12: Image reconstruction using round pipeline sensors

As shown by Figure 12 (a), with the single-plane round pipeline sensor, the phantoms cannot be correctly reconstructed either in position or shape (e.g. a sphere in centre). With the twin-plane round pipeline sensor, the situation can be improved as shown in Figure 12 (b). The position of phantom is correct, and the shape of phantom (e.g. a sphere in centre) is improved and close to the real phantom. It means the cross measurements between twin planes provide information in Z direction, and 3D images can be obtained.

5.4 Reconstruction using multiple projection data

Figure 13 shows comparison between the true 3D 54-electrode sensor (see Figure 5 (b)) and the 36-electrode sensor without top and bottom electrodes (see Figure 4 (a)). In the 36-electrode sensor, the top and bottom electrodes are removed. To obtain a reasonable 3D image, both the number of planes of electrodes needs to be increased and more iteration are needed. Also the relaxation factor must be chosen to be small to deal with the ill-posed problem and to ensure the convergence.

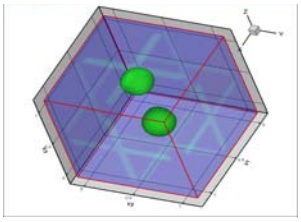

(a) Using true 3D 54-electrode sensor (Figure 5 (b)) providing complete data and Landweber iteration (1 time)

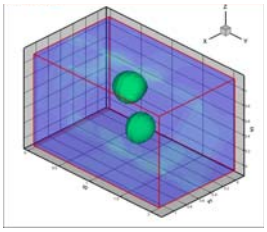

(b) Using 36-electrode sensor without top and bottom electrodes (Figure 4 (a)) providing incomplete data and Landweber iteration (100 times)

Figure 13: Reconstruction of two spheres

6. Conclusions

Usually an ECT system generates 2D images of a cross section. In the past, some researchers generated 3D images, either by stacking 2D images together as 2½D images or using incomplete and small number of measurement data. This paper has presented true 3D images reconstructed using complete measurement data. Both LPB and the Landweber iteration algorithm as simplified linear methods have been implemented for image reconstruction. A full nonlinear algorithm has been implemented based on a regularised Gauss-Newton method. For comparison purposes, various 3D ECT sensors with different number of electrodes and different projections have been investigated for reconstructing permittivity distribution in 3D. A single-plane sensor may be used to reconstruct 3D images but the image quality is poor. The image quality can be improved by using a multiple-plan sensor. If the measurement data are available from all projections, i.e. complete measurement data in full 3D, good images can be reconstructed. From the practical point of view, it is interesting to see the potential applications of the full 3D ECT sensor.

Owing to the large number of cells, full 3D image reconstruction process is slow, even with a linear algorithm, taking 2 minutes to reconstruct one image. Also, the full nonlinear image reconstruction requires extensive computation, due to the solution to the forward problem in each iteration and re-calculation of the Jacobian matrix. Currently, it can be used as a tool for 3D ECT, but off-line operation only. Fully nonlinear algorithm and full 3D ECT data are major advances reported in this paper. Further study is required in advanced computation, such as parallel computing, efficient linear solvers to make online 3D imaging possible.

References

[1] T Dyakowski, L F C Jeanmeure, W B Zimmerman and W Clark, Direct flow-pattern identification using electrical capacitance tomography, *Experimental Thermal and Fluid Science, 26 (6-7), 2002, pp 763-773*

[2] Ansoft, www.ansoft.com

[3] S Gomez, O Michiyo, C Gamio and A Fraguela, Reconstruction of capacitance tomography images of simulated two-phase flow regimes, *Applied Numerical Mathematics, 46, 2003, pp 197-208*

[4] S M Huang, A Plaskowski, C G Xie and M S Beck, Tomographic imaging of two-component flow using capacitance sensors, *Journal of Physics E: Science, vol. 1989, pp 173-177*

[5] W Q Yang and S Liu, Electrical capacitance tomography with square sensor, *Electronic Letters, 35, 1999, pp 295-296*

[6] M Soleimani and W R B Lionheart, Nonlinear image reconstruction in electrical capacitance tomography using experimental data, *Meas. Sci. Technol. 16, 2005, pp 1987-1996*

[7] M Soleimani, Numerical modelling and analysis of the forward and inverse problems in electrical capacitance tomography, *Int. J. for Information and Systems Sciences, 1 (2), 2005, pp 193-207*

[8] M Soleimani, Three dimensional electrical capacitance imaging, *Insight, Non-Destructive Testing and Condition Monitoring, 48 (10), 2006, pp 613-617*

[9] W Warsito and L S Fan, Neural network based multi-criterion optimization image reconstruction technique for imaging two- and three-phase flow systems using electrical capacitance tomography, *Meas. Sci. Technol. 12, 2001, pp 2198-2210*

[10] W Warsito and L S Fan, Dynamics of spiral bubble plume motion in the entrance region of bubble columns and three-phase fluidized beds using 3D ECT, *Chemical Engineering Science, 60 (22), 2005, pp 6073-6084*

[11] R A Williams and M S Beck, Process Tomography, Principles, Techniques and Applications, *Butterworth-Heinemann, Oxford, UK, 1995*
[12] W Q Yang, Calibration of capacitance tomography systems: a new method for setting system measurement range*, Meas. Sci. Technol., 7, 1996, pp L863-L867*
[13] W Q Yang, D M Spink, T A York and H McCann, An image-reconstruction algorithm based on Landweber's iteration method for electrical-capacitance tomography*, Meas. Sci. Technol. 10, 1999, pp 1065-1069*
[14] W Q Yang and L H Peng, Image reconstruction algorithms for electrical capacitance tomography, Meas. Sci. Technol., 14, 2003, pp R1-R13
[15] R Wajman, R Banasiak, L Mazurkiewicz, T Dyakowski and D Sankowski, Spatial imaging with 3D capacitance measurements, Meas. Sci. Technol., 17, 2006, pp 2113-2118
[16] R Kupferman, Numerical study of the axisymmetric Couette-Taylor problem using a fast high-resolution second-order central scheme, SIAM Journal of Scientific Computing, 20, 1998, pp 858-887

[1] William Lee Innovation Centre, School of Materials, The University of Manchester, PO Box 88, Manchester M60 1QD, UK, Email: M.Soleimani-2@manchester.ac.uk
[2] School of Electrical and Electronic Engineering, The University of Manchester, PO Box 88, Manchester M60 1QD, UK, E-mail: Yi.Li@postgrad.manchester.ac.uk